A neural network approach to the combined multi-objective optimization of the thermodynamic cycle and the radial inflow turbine for Organic Rankine cycle applications

Article *in* Applied Energy · January 2019

DOI: 10.1016/j.apenergy.2019.01.035

CITATIONS
6

READS
713

3 authors:

Laura Palagi
Sapienza University of Rome
65 PUBLICATIONS **640** CITATIONS
SEE PROFILE

Sciubba Enrico
Sapienza University of Rome
241 PUBLICATIONS **4,817** CITATIONS
SEE PROFILE

Lorenzo Tocci
Sapienza University of Rome
14 PUBLICATIONS **166** CITATIONS
SEE PROFILE

A Neural Network approach to the combined multi-objective optimization of the thermodynamic cycle and the radial inflow turbine for Organic Rankine Cycle applications

Laura Palagi[a], Enrico Sciubba[b], Lorenzo Tocci[b,c,*]

[a]*Department of Computer, Control, and Management Engineering, "La Sapienza" University of Rome, Via Ariosto 25, 00185 Rome, Italy*
[b]*Department of Mechanical and Aerospace Engineering, "La Sapienza" University of Rome, Via Eudossiana 18, 00184 Rome, Italy*
[c]*Entropea Labs, 2a Greenwood Road, E81AB London, UK*

Abstract

An optimization model based on the use of Neural Network surrogate models for the multi-objective optimization of small scale Organic Rankine Cycles is presented, which couples the optimal selection of the thermodynamic parameters of the cycle with the main design parameters of In-Flow Radial turbines. The proposed approach proved well suited in the resolution of the highly non-linear constrained optimization problems, typical of the design of energy systems. Indeed the use of a surrogate model allows to adopt gradient based methods that are computationally more efficient and accurate than conventional derivative-free optimization algorithms.

The intensive numerical experiments demonstrate that assuming a constant efficiency for the In-Flow Radial turbine leads to an error in the evaluation of the performance of the system of up to 50 % and that the optimization approach proposed improves the accuracy of the solution and it reduces the computational time required to reach it by two orders of magnitude. An holistic approach in which the turbine and the thermodynamic cycle are designed simultaneously and the use of multi-objective optimization proved to be essential for the design of Organic Rankine cycles that satisfy both size and performance criteria.

Keywords: Artificial Neural Networks, ORC, ANN, Radial inflow turbine, Turbine efficiency

1. Introduction

Organic Rankine Cycle (ORC) is a consolidated technology to exploit thermal energy from wasted heat in low/medium temperature (400 to 700 K) range. Although the ORC

*Corresponding author
Email addresses: laura.palagi@uniroma1.it (Laura Palagi), enrico.sciubba@uniroma1.it (Enrico Sciubba), lorenzo.tocci@uniroma1.it (Lorenzo Tocci)

technology has been widely installed to produce power in the MW range [1], the installation of ORC machines of power in the kW range still finds little practical application. In fact, when scaling down ORC systems, additional design issues arise which still limit the widespread availability of the technology. Particular effort has been recently expended by researchers to try to optimize the performance of ORC systems in the production of power in the kW range. Tocci et al. [2], in their techno-economic review of ORC applications, stated that particular attention needs to be taken when designing the turbine, in that its performance plays a crucial role in the definition of the overall efficiency of ORC systems; therefore, a preliminary design of the turbine needs to be considered in the process of optimization of the thermodynamic parameters of the cycle.

Even though it is usual practice to define the thermodynamic cycle as a first step and subsequently to design the turbine, recently, researchers started to consider the effect of the thermodynamic parameters of ORC cycles on the performance of the turbine at an early design stage. Uusitalo et al. [3] addressed the subject of combining the design of the ORC cycle's thermodynamics and of the turbine for low power applications, discussing the performance of different working fluids. Ventura and Rowlands [4] proposed a tool to couple the design of radial turbines to the selection of the thermodynamic parameters of the cycle. La Seta et al. [5] derived an optimization tool to carry out the simultaneous optimization of both the cycle's and the turbine's design. Zhai et al. [6] developed an optimization tool for the simultaneous design of the ORC cycle and of the radial turbine using genetic algorithms. Lazzaretto and Manente [7] proposed an optimization procedure of the thermodynamic cycle of the ORC in which a specific correlation for the efficiency of the turbine is included: they derived correlations for both radial and axial turbines.

The combined optimization of the thermodynamic parameters of the cycle and of the design parameters of the turbine implies the need to solve a highly non-linear constrained optimization problem, which requires the use of thermodynamic libraries to calculate the thermo-physical properties of the fluids involved in the transformations. It is usual practice in the energy field to use derivative-free optimization methods, such as artificial bees colonies [8] and genetic algorithms [9], to solve highly nonlinear black-box optimization problems. However, derivative-free optimization algorithms have the disadvantage of being intrinsically slow, due both to the high computational cost of functions' evaluations and to the large number of such evaluations. In addition, they are less accurate than the algorithms based on the gradient method, i.e. those that use the derivative of the objective function and of the constraints during the optimization process.

In this work, Neural Networks are used to derive surrogate models and to overcome the limitation of derivative-free optimization algorithms. Artificial Neural Networks (ANNs) allow to derive approximated mathematical models of the nonlinear system based on samples. The resulting model can be conveniently applied to the combined optimization of the thermodynamic parameters of the ORC cycle and of the design parameters of the turbine. The use of Neural Networks to improve optimization processes has been discussed in previous works [10]. ANN models provide an intrinsically continuous and differentiable correlation function that allows for the use of analytical gradient methods for its optimization [11]. The use of gradient methods, as opposed to derivative-free methods commonly used in ORC

optimization problems, allows to reach more accurate results in an amount of time that is one order of magnitude smaller with respect to that of derivative-free optimization algorithms [12]. To the authors' knowledge, no one has ever applied the proposed methodology to the combined optimization of the thermodynamic cycle and of the design of the turbine of ORC systems. This paper aims at presenting an optimization tool specifically derived for the multi-objective optimization of small scale ORC systems, in which a novel model of radial in-flow turbines coupled to a model of the thermodynamic cycle is converted into a set of ANNs to improve the optimization performance of the highly non linear model of the system.

The paper is organized as follows. Section 2 describes the architecture of the neural network implemented, which has been developed using the platform TensorFlow [13]. Section 3 presents the thermodynamic model of the ORC cycle, the analytical model to derive the performance of IFR turbines, the model to preliminary estimate the size of the heat exchangers and the formulation of the optimization problem to be solved. Section 4 investigates the influence of the thermodynamic parameters of the ORC cycle on the performance of IFR turbines. Section 5 applies the ANN based optimization model to the combined optimization of the thermodynamic parameters of the cycle and of the design parameters of the IFR turbine of a small scale ORC system. Section 6 summarizes the results of the study.

2. Neural networks

A learning machine can be described as a regression tool capable of deriving a mathematical model by means of a set of samples representing the process and available in the form $(\mathbf{x}^p, \bar{y}^p)$, for $p = 1, \ldots, P$, where $\mathbf{x}^p \in \mathbb{R}^n$ represents the features of the input and $\bar{y}^p \in \mathbb{R}^m$ the corresponding outputs. These samples can be derived as measures of experiments or using numerical thermodynamic tools. Among learning machines, Artificial Neural networks (ANN) are often selected, since they proved reliable in many different tasks [14]. The aim of an ANN model is to define a function $y : \mathbb{R}^n \to \mathbb{R}^m$ as a "good" approximation of the unknown function underlying the process. The type of function and the parameters settings are defined through a learning procedure briefly described below. The basic ANN architecture is known as the Multi Layer Perceptron (MLP) and it is composed by units (neurons) organized in layers forward-connected to each other. As a matter of example in Figure 1 (a) a representation of an ANN is reported where the nodes represent the neurons and the arcs represent the weighted synaptic connections among neurons.

The main elements characterizing an ANN are:

- an input layer (IL), that receives the training examples;
- one or more intermediate layers, called *hidden* layers (HL);
- an output layer (OL), which consists of as many neurons as the number of outputs of the network.

An ANN consisting of a unique hidden layer, as e.g. in Figure 1, is called *shallow network* whereas it is called *deep network* otherwise. Each unit of the HL is characterized by the activation function g, which acts as an on-off trigger on a weighted combination of the outputs of the neurons in the preceding layer, and a bias b_j; each connection from input i to neuron j of the HL is characterized by a weight w_i^j as shown in Figure 1 (b); the arc from the hidden neuron j to the output neuron are weighted by w_o^j.

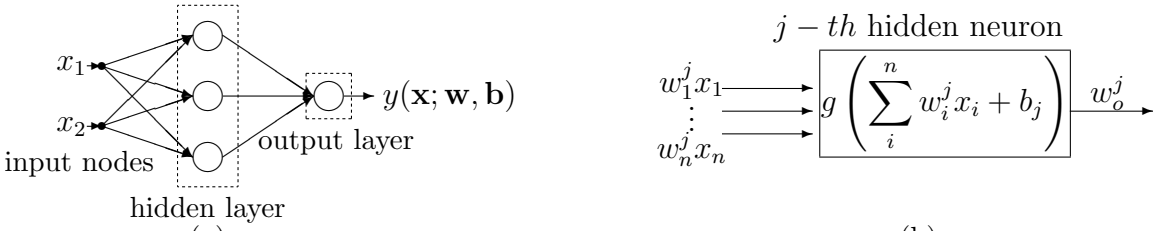

Figure 1: (a) ANN with one hidden layer and one output; (b) internal structure of the j-th neuron of the hidden layer.

The number of the hidden layers L and the number of neurons m^ℓ in each HL $\ell = 1, \ldots, L$ together with the activation function g of the neurons are user-dependent parameters. Once they are fixed, the output of the ANN network is obtained by forward propagation of the input. In the case of a shallow network with one output, it takes the following form:

$$y(\mathbf{x};\mathbf{w},\mathbf{b}) \;\; = \sum_j^m w_o^j g\left(\sum_i^n w_i^j x_i + b_j\right) \tag{1}$$

where $\mathbf{w} = \{w_o^j, w_i^j\}_{i=1,\ldots,j=1,\ldots,m}$ and $\mathbf{b} = \{b_j, b_o\}_{j=1,\ldots,m}$ are respectively the weights and the biases of the neurons.

All the parameters $\mathbf{w}, \mathbf{b}$ that appear in Eq. (1) are "learned" through a *training* process that consists in the solution of the minimization problem described by Eq. (2):

$$\min_{\mathbf{w},\mathbf{b}} E(\mathbf{w},\mathbf{b}) \;\; = \frac{1}{2}\sum_p^P \|\bar{y}_p - y(\mathbf{x}_p;\mathbf{w},\mathbf{b})\|^2 \tag{2}$$

3. The mathematical models

Section 3 reports the description of the mathematical models considered in this work for the design of small scale ORC systems. The models have been coded using MATLAB [15] whereas the thermodynamic properties of the fluids have been calculated using the thermodynamic library REFPROP [16]. Figure 2 shows the thermodynamic transformations of a regenerated ORC system on the specific entropy - Temperature diagram. Table 1 provides a brief description of the processes that take place in each of the components of the system.

Section 3.1 presents the thermodynamic model of the ORC cycle. Section 3.2 describes the analytical model for the preliminary design of the IFR turbine. Section 3.3 reports the

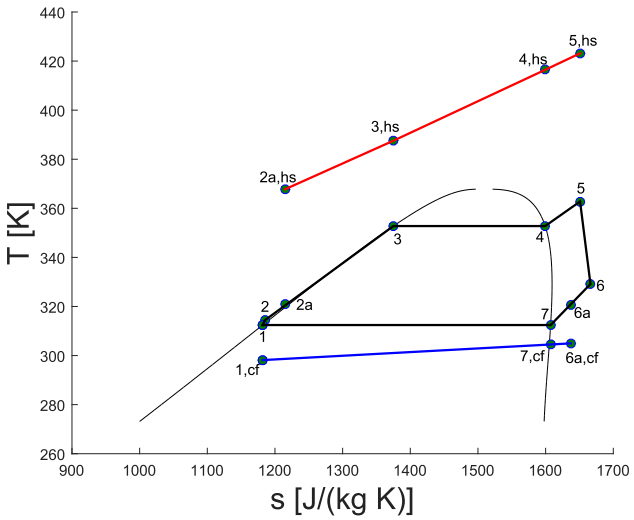

Figure 2: T-s diagram of an ORC thermodynamic cycle.

Table 1: Transformations of the cycle.

Transformation	**Component**	**Description**
1 - 2	Pump	Fluid pressurized by the pump
2a - 3	Pre-heater	Pressurized fluid heating
3 - 4	Evaporator	Pressurized fluid vaporization
4 - 5	Super-heater	Pressurized fluid super-heating
5 - 6	Turbine	Expansion process
6 - 6a	Regenerator	Heat recovery to pre-heat the fluid at the pump outlet
6a - 1	Condenser	Fluid condensation

calculations performed to preliminary assess the size of the heat exchangers of an ORC system, based on the ϵ - Net Transfer Unit (NTU) method. Section 3.4 reports the formulation of the optimization problem to be solved using the proposed machine learning approach.

3.1. Thermodynamic model of the Organic Rankine Cycle

The thermodynamic model of the ORC is based on the mass conservation equations and the energy balance equations applied to each component of the system. Eq. (3) to (10) are

representative of the model implemented.

$$\dot{m}_{hs} = const \tag{3}$$
$$\dot{m}_{wf} = const \tag{4}$$
$$\dot{m}_{cf} = const \tag{5}$$
$$\dot{m}_{hs} \cdot (h_{5,hs} - h_{2a,hs}) = \dot{m}_{wf} \cdot (h_5 - h_{2a}) \tag{6}$$
$$P_{turbine} = \eta_{turbine} \cdot \dot{m}_{wf} \cdot (h_5 - h_6) \tag{7}$$
$$\dot{m}_{wf} \cdot (h_{6a} - h_1) = \dot{m}_{cf} \cdot (h_{6a,cf} - h_{1,cf}) \tag{8}$$
$$\dot{m}_{wf} \cdot (h_6 - h_{6a}) = \dot{m}_{wf} \cdot (h_{2a} - h_2) \tag{9}$$
$$P_{pump} = \dot{m}_{wf} \cdot (h_2 - h_1)/\eta_{pump} \tag{10}$$
$$RD = \frac{h_6 - h_{6a}}{h_6 - h_7} \tag{11}$$

The subscripts refer to the thermodynamic points depicted in Figure 2, where $\dot{m}_{hs}$, $\dot{m}_{wf}$ and $\dot{m}_{cf}$ are the mass flow rates of the heat source, of the working fluid and of the cooling fluid respectively, RD is the degree of regeneration, $\eta_{turbine}$ and η_{pump} are the isentropic efficiencies of the turbine and of the pump.

3.2. Analytical model of the in-flow radial turbine

The In-Flow Radial (IFR) turbine model presented in this section is based on the calculation of the velocity triangles (quasi-two dimensional model). The model requires as input the thermodynamic parameters of the expansion process, namely inlet temperature, inlet pressure and outlet pressure, and provides in output the isentropic efficiency of the machine.

Figure 3 shows the sections in which the IFR turbine is divided.

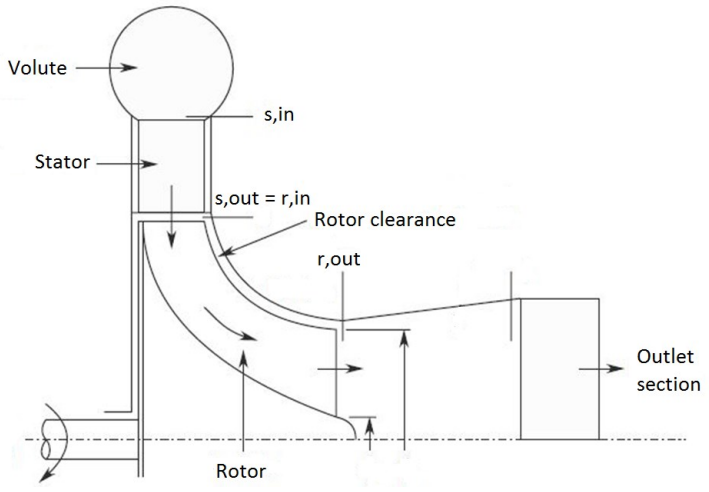

Figure 3: In-Flow Radial (IFR) turbine.

As shown in Figure 3, an IFR turbine is composed of a volute that distributes the fluid around the statoric blades; a statoric row of blades (nozzle vanes) that partially convert

pressure energy into kinetic energy; a row of rotoric blades that extract the energy deriving from the expansion of the working fluid, transferring it to the rotating shaft as mechanical energy. The design of an IFR turbine consists in the definition of the geometry of the various sections of the machine. To this end, some parameters have been kept constant in the IFR turbine design, using values suggested by experience in turbomachinery to maximize the performance of IFR turbines [17]. Table 2 lists the constant inputs used for the design of the IFR turbine:

Table 2: Inlet design parameters for the IFR turbine design

Parameter	**Value**
$\psi_{r,out}$	0
ϕ_c	0.25
$V_{v,in}$	50 m/s
$\frac{D_{s,in}}{D_{r,in}}$	1.3
$\frac{b_{r,in}}{D_{r,in}}$	0.02

where $\psi_{r,out}$ is the head coefficient at the outlet section of the rotor, ϕ_c is the flow coefficient of Chen and Baines, $V_{v,out}$ is the velocity of the fluid at inlet section of the volute, $D_{s,in}/D_{r,in}$ is the ratio between the inlet diameter of the stator and the rotor and $b_{r,in}/D_{r,in}$ is the ratio of the thickness of the blades to the diameter at the inlet section of the rotor. In addition to the constant values listed in Table 2, the pressure at the inlet of the volute ($p_{v,in}$), the temperature at the inlet of the volute ($T_{v,in}$), the pressure at the outlet of the rotor ($p_{r,out}$), the mass flow rate of the working fluid ($\dot{m}_{wf}$), the specific speed (n_s), the specific diameter (d_s) and a first tentative isentropic efficiency (η_{is}) are provided as input variables. The thermodynamic conditions at the inlet of the IFR turbine are fully defined, in that temperature and pressure are known from the calculation of the thermodynamic cycle. The first tentative value of the isentropic efficiency (η_{is}) is used to calculate the enthalpy at the outlet of the rotor of the turbine and hence, the Euler Work (W_{Euler}) that the turbine provides, using Eq. (12):

$$W_{Euler} = \eta_{is} \cdot (h_{v,in} - h_{r,out,is}) \tag{12}$$

The power output of the turbine ($P_{turbine}$) is calculated using Eq. (13):

$$P_{turbine} = \dot{m}_{wf} \cdot W_{Euler} \tag{13}$$

The specific speed of the IFR turbine (n_s) is used to calculate the rotational speed ($\omega_{turbine}$, Eq. (14)):

$$\omega_{turbine} = \frac{n_s \cdot W_{Euler}^{0.75}}{Q_{r,out}^{0.5}} \tag{14}$$

Where $Q_{r,out}$ is the volumetric flow rate at the outlet of the rotor, defined as:

$$Q_{r,out} = \dot{m}_{wf}/\rho_{r,out} \tag{15}$$

The specific diameter of the IFR turbine (d_s) is used to calculate the diameter of the rotor of the IFR turbine at the inlet section ($D_{r,in}$):

$$D_{r,in} = \frac{d_s \cdot Q_{r,out}^{0.5}}{W_{Euler}^{0.25}} \tag{16}$$

and the height of the blade at the inlet of the rotor ($b_{r,in}$) is defined considering the ratio $\frac{b_{r,in}}{D_{r,in}}$ reported in Table 2:

$$b_{r,in} = \frac{b_{r,in}}{D_{r,in}} \cdot D_{r,in} \tag{17}$$

The peripheral velocity at the inlet section of the rotor ($\vec{U}_{r,in}$) is equal to:

$$\vec{U}_{r,in} = \omega_{turbine} \cdot \frac{D_{r,in}}{2} \tag{18}$$

Once $\vec{U}_{r,in}$ is known, the head coefficient at the inlet of the turbine ($\psi_{r,in}$) is calculated as:

$$\psi_{r,in} = W_{Euler}/\vec{U}_{r,in}^2 \tag{19}$$

The definition of the parameters at the inlet section of the rotor is completed using the chart defined by Rohlik, which reports the optimal inlet angle of the flow into the rotor of the IFR turbine as a function of the specific speed. Figure 4 displays the Rohlik's chart [18].

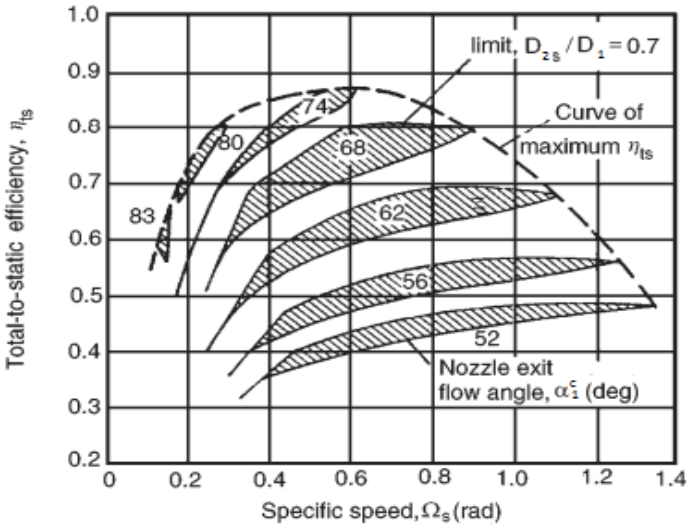

Figure 4: Rohlik's chart for the definition of the optimal nozzle exit angle.

At this stage, the velocity triangle at the inlet of the rotor can be evaluated. The velocity triangle of the rotor at the outlet section is calculated using the flow coefficient (ϕ_c, see Table 2) as defined by Chen and Baines [19].

The flow coefficient, as defined by Chen and Baines (ϕ_c) is reported in Eq. (20).

$$\phi_c = \vec{V}_{r,out}/\vec{U}_{r,in} \tag{20}$$

Knowing the absolute velocity at the outlet section of the rotor ($\vec{V}_{r,out}$) and the head coefficient at the outlet section of the rotor ($\psi_{r,out}$, see Table 2), it is possible to define the velocity triangle at the outlet of the IFR turbine's rotor.

At this point, the number of blades of the rotor (Z_r) is calculated using Eq. (21).

$$Z_r = \pi/30 \cdot (100 - \alpha_{Rohlik}) \cdot tan(\alpha_{Rohlik}) \tag{21}$$

Finally, the stator is designed using the diameter ratio listed in Table 2 ($D_{s,in}/D_{r,in}$) and assuming that the fluid enters the stator radially.

The geometry is now fully defined and the losses in the different sections of the IFR turbine can be evaluated to calculate the value of the isentropic efficiency of the IFR turbine. In this work, the following losses have been taken into account:

- Rotor losses, comprehending tip clearance, secondary, friction and exit kinetic losses;
- Nozzle losses, which depend on friction;
- Volute losses.

The losses in the different sections of the machine reduce the available enthalpy drop of the working fluid that is transferred to the rotating shaft in form of mechanical energy. Therefore, the isentropic efficiency of the turbine is calculated as in Eq. (22):

$$\eta_{is} = \frac{W_{Euler} - \Delta h_{losses}}{W_{Euler}} \tag{22}$$

where Δh_{losses} is the sum of the losses in the different sections of the IFR turbine:

$$\Delta h_{losses} = \Delta h_{losses,r} + \Delta h_{losses,s} + \Delta h_{losses,v} \tag{23}$$

An in depth analysis of the losses occurring in IFR turbines is beyond the scope of this work. One interested in the detailed analysis of the losses model considered in this paper, is referred to the work of Rahbar et al. [20], who analyzed in detail the nature of the losses of an IFR turbine for ORC applications.

Once the isentropic efficiency of the turbine is computed, the design process is iterated using the new value for the isentropic efficiency of the turbine. The process stops when the discrepancy between the tentative value of the efficiency and that of the calculated efficiency is negligible.

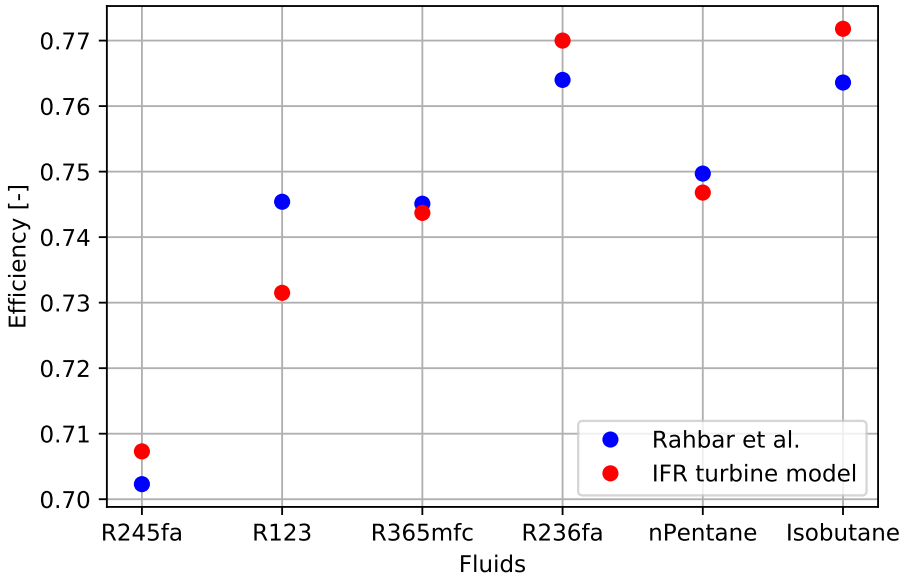

Figure 5: Validation of the IFR turbine model against the results of Rahbar et al. [20].

The model of the IFR turbine presented in Section 3.2 has been validated against the results presented in the work of Rahbar et al. [20]. Figure 5 reports the validation of the IFR turbine model.

One may notice that the prediction of the isentropic efficiency of the IFR turbine model presented in this work is in accordance to that of the model presented in [20].

The IFR turbine model has been also validated against experimental studies. The results are displayed in Figure 6:

The validation against the experimental results reported in Figure 6 shows that the IFR turbine model proposed in this paper is able to estimate the efficiency of IFR turbines with a good degree of accuracy.

3.3. Calculation of the size of the heat exchangers

In this work an estimation of the size of the heat exchangers is expressed using the UA parameter, which has been calculated using the $NTU - \epsilon$ method. Even though a complete design of the heat exchangers has not been performed in this work, the UA parameter provides a good understanding of the size of the heat exchangers of which an ORC system is composed. In an ORC system, heat transfer takes place in the evaporator, the regenerator and the condenser. The evaporator has been divided into pre-heating (2a - 3, see Figure 2), vaporization (3 -4) and super heating (4 - 5) sections whereas the condenser has been divided into de-super heating (6a - 7), condensation (7 - 8) and sub-cooling (8 - 1). The UA parameter has been calculated for each of the aforementioned sections and for the regenerator. Finally the sum of each segment provides the sum of the UA parameter of the

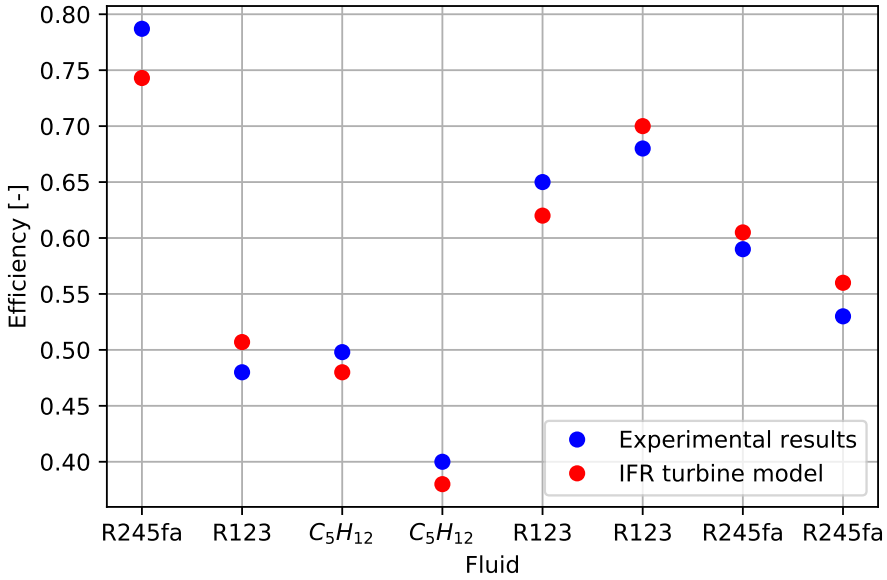

Figure 6: Validation of the IFR turbine model against the experimental results reported in Bao and Zhao [21].

heat exchangers (UA_{sum}). The $NTU - \epsilon$ method is an established methodology: interested readers are referred for example to [22] for a detailed description of the procedure.

3.4. Definition of the optimization problems

The mathematical models described in sections 3.1, 3.2 and 3.3 have been used in combination to solve the optimization problems described in this Section. The aim of this work is to define an ANN based optimization tool that can be used by process engineers to select the optimal thermodynamic parameters of an ORC cycle, considering the effect of the thermodynamic parameters selected on the performance of the IFR turbine. Three different optimization problems have been solved in this work, namely the maximization of the net power output of the ORC system (P_{cycle}), the maximization of the cycle's efficiency (η_{cycle}) and the minimization of the size of the components (UA_{sum}).

The optimization model (24) displays the different objective functions and the constraints

considered in the analysis.

$$
\begin{aligned}
\max_{\mathbf{x}\in\Omega} \quad & P_{cycle} \\
\max_{\mathbf{x}\in\Omega} \quad & \eta_{cycle} \\
\min_{\mathbf{x}\in\Omega} \quad & UA_{sum} \\
\text{subject to} \quad & T_i - T_{i,cf} \geq \Delta T\,,\ i = 1,7 \\
& T_{6a} - T_{6a,cf} \geq \Delta T \\
& T_8 - T_{8,cf} \geq \Delta T \\
& T_{2a,hs} - T_{2a} \geq \Delta T \\
& T_6 - T_{2a} \geq \Delta T \\
& T_{6a} - T_2 \geq \Delta T \\
& T_{i,hs} - T_i \geq \Delta T\,,\ i = 3,5 \\
& T_{2a,hs} - T_2 \geq \Delta_T \\
& h_{2a} \leq h_3 \\
& T_{2a} \geq T_2 \\
& T_{6a} \leq T_6 \\
& T_{6a} \geq T_7 \\
& T_{2a,hs} \geq T_{limit,hs}
\end{aligned}
\tag{24}
$$

where $\Omega \subseteq \mathbb{R}^7$ is a set representing lower and upper bounds on the variables, ΔT is the minimum pinch temperature difference allowed in the heat exchangers, T_8 and $T_{8,cf}$ are respectively the temperature of the working fluid and of the cooling source at the end of the condensation process, P_{cycle} and η_{cycle} are explicitly reported in Eq. (25) and (26).

$$P_{cycle} = P_{turbine} - P_{pump} \tag{25}$$

$$\eta_{cycle} = \frac{P_{cycle}}{\dot{m}_{wf} \cdot (h_5 - h_{2a})} \tag{26}$$

The optimization has the objective to define the optimal thermodynamic parameters of the cycle and the optimal design parameters of the IFR turbine at the same time. Table 3 reports the decision variables considered in this work:

In Table 3, $\dot{m}_{wf}$ is the mass flow rate of the working fluid, T_4 and T_7 are the vaporization and condensation temperatures of the cycle (see Figure 2), ΔT_{sh} is the superheat, RD is the degree of regeneration, n_s is the specific speed of the IFR turbine and d_s is the specific diameter of the turbine at the inlet section of the rotor.

The general multi-objective optimization problem can be expressed as:

Table 3: Decision variables of the optimization problem.

Independent Parameter	SI unit
$\dot{m}_{wf}$	[kg/s]
T_4	[K]
$\Delta T_{sh} = T_5 - T_4$	[K]
T_7	[K]
RD	[-]
n_s	[-]
d_s	[-]

$$\begin{aligned} \min_{\mathbf{x}\in\Omega} \quad & f_j(x)\,,\ j = 1,\ldots,3 \\ \text{subject to} \quad & c_i(x) \leq 0\,,\ i = 1,\ldots,15 \end{aligned} \tag{27}$$

where f_j represents the three objective functions and c_i represents the sixteen constraints in the same order as they appear in Eq. (24).

4. Effect of the thermodynamic parameters of the cycle on the performance of the turbine

Section 4 provides an investigation of the effect of the thermodynamic parameters of the ORC cycle on the efficiency of the IFR turbine, to quantify the advantages of the model proposed in this paper over a simplified model that considers a constant value for the isentropic efficiency of the IFR turbine. The objective of this section is twofold. First, the impact of the parameters listed in Table 3 on the isentropic efficiency of the turbine is investigated. Second, the discrepancy in evaluating the performance of the ORC system considering a constant isentropic efficiency of 0.75 for the IFR turbine and taking into account the effect of the thermodynamic parameters on the efficiency of the IFR turbine is addressed. To this end, the parameters listed in Table 3 have been varied over a wide range and the results on the performance of the system are discussed. The name of the working fluid implemented in this work cannot be disclosed for confidentiality reasons.

Figure 7 reports the IFR turbine isentropic efficiency as a function of the specific speed (n_s) and of the specific diameter (d_s).

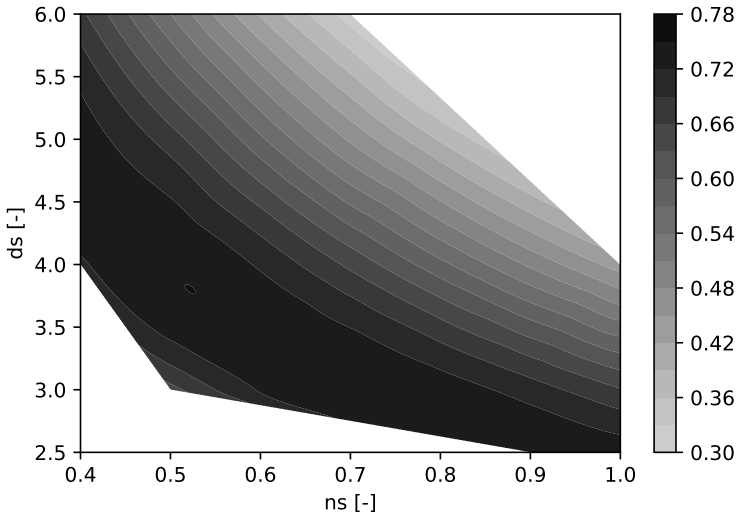

Figure 7: IFR turbine efficiency as a function of the specific speed (n_s) and of the specific diameter (d_s).

From Figure 7 it is possible to notice that the maximization of the efficiency of the IFR turbine is reached from the selection of an optimal pair of specific speed and specific diameter. Figure 7 shows that higher values of the specific speed result in a better efficiency when coupled with lower values of the specific diameter and viceversa, which is consistent with all accepted performance charts.

Figure 8 reports the isentropic efficiency of the IFR turbine as a function of the vaporization temperature for various values of the superheat, for fixed mass flow rate (0.8 kg/s), condensation temperature (313.15 K), degree of regeneration (0.5), specific speed (0.8) and specific diameter (3).

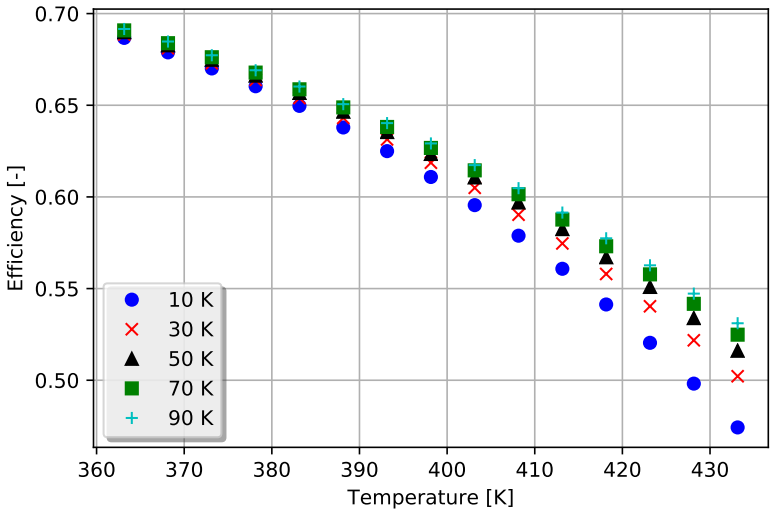

Figure 8: Isentropic efficiency of the IFR turbine as a function of the vaporization temperature for various values of the superheat, for fixed mass flow rate (0.8 kg/s), condensation temperature (313.15 K), degree of regeneration (0.5), specific speed (0.8) and specific diameter (3)..

Figure 8 shows that the isentropic efficiency of the IFR turbine decreases when the vaporization temperature of the ORC cycle is increased. This is an important effect to keep into account. On one hand, an increase in the vaporization temperature has a negative impact on the performance of the IFR turbine. On the other hand, the higher the vaporization temperature the higher the efficiency of the ORC cycle, for a constant performance of the turbine. A good trade off between the isentropic efficiency of the turbine and the efficiency of the thermodynamic cycle needs to be found, which highlights the need for the combined optimization of the two parameters. In addition, Figure 8 shows that the increase of the superheat is beneficial for the performance of the turbine, which is a tendency well known by designers. The gain in efficiency for the IFR turbine due to an increase in the superheat is higher when the vaporization temperature of the cycle is higher. However, one may notice that the effect of the superheat on the performance of the turbine is negligible when compared to that of the vaporization temperature of the cycle.

Figure 9 reports the isentropic efficiency of the IFR turbine as a function of the condensation temperature for different values of the vaporization temperature, for fixed mass flow rate (0.6 kg/s), superheat (50 K), degree of regeneration (0.7), specific speed (0.6) and specific diameter (3).

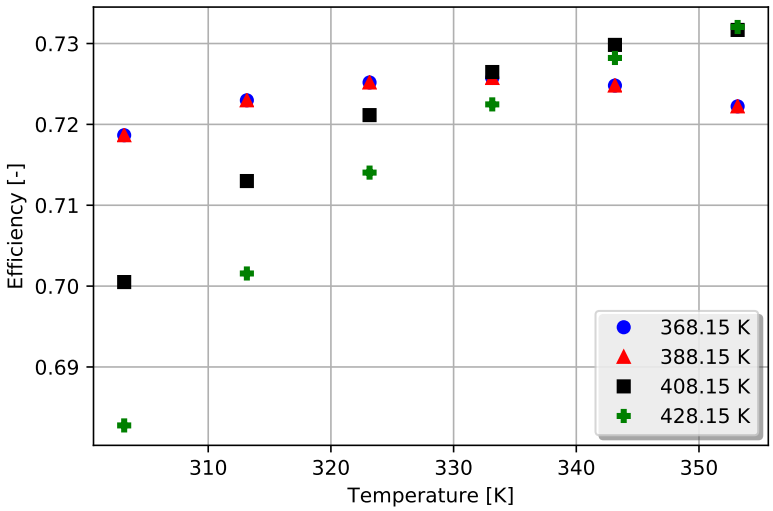

Figure 9: Isentropic efficiency of the IFR turbine as a function of the condensation temperature for various values of the vaporization temperature, for fixed mass flow rate (0.6 kg/s), superheat (50 K), degree of regeneration (0.7), specific speed (0.6) and specific diameter (3).

Figure 9 shows that no linear correlation exists between the performance of the IFR turbine and the temperature difference between the vaporization and the condensation processes. In fact, when the condensation temperature is low, the IFR turbine benefits from a low value of the vaporization temperature. On the contrary, for high values of the condensation temperature, the isentropic efficiency of the turbine increases for higher vaporization temperatures. Figures 7 to 9 demonstrate the nonlinear impact of the thermodynamic parameters of the ORC cycle and of the design parameters of the turbine on the performance of the IFR turbine. The rest of Section 4 investigates the error that derives from considering a constant value of 0.75 for the isentropic efficiency of the IFR turbine with respect to the use of a more accurate calculation of the performance of the turbine using the model proposed in Section 3.

Figure 10 reports the net power (P_{cycle}) and the efficiency (η_{cycle}) of the ORC cycle as a function of the vaporization temperature, for fixed mass flow rate (0.75 kg/s), superheat (50 K), condensation temperature (313.15 K), degree of regeneration (0.75), specific speed (0.6) and specific diameter (3).

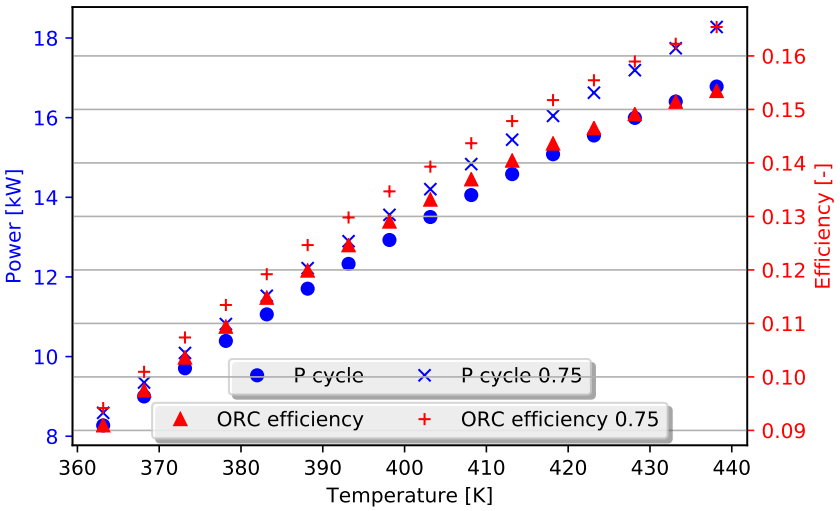

Figure 10: ORC cycle net power (P_{cycle}) and efficiency (η_{cycle}) as a function of the vaporization temperature, for fixed mass flow rate (0.75 kg/s), superheat (50 K), condensation temperature (313.15 K), degree of regeneration (0.75), specific speed (0.6) and specific diameter (3).

The full dots in Figure 10 represent the values calculated using the model proposed in Section 3 while the crosses represent the values calculated considering a constant efficiency for the IFR turbine. Figure 10 shows that the efficiency of the cycle and the net power output are overestimated when assuming a constant value for the efficiency of the turbine. The discrepancy between the two models is higher for higher values of the vaporization temperature. The efficiency of the ORC increases with the vaporization temperature. In fact, increasing the vaporization temperature implies that the heat is provided to the ORC at a higher average temperature, which has a positive effect on the efficiency of the cycle. The net power of the cycle increases when the vaporization temperature increases. This is due to the increase in the difference between the work provided by the turbine with respect to that absorbed by the pump.

Figure 11 reports the net power (P_{cycle}) and the efficiency (η_{cycle}) of the ORC cycle as a function of the condensation temperature, for fixed mass flow rate (0.7 kg/s), superheat (50 K), vaporization temperature (368.15 K), degree of regeneration (0.9), specific speed (0.6) and specific diameter (3).

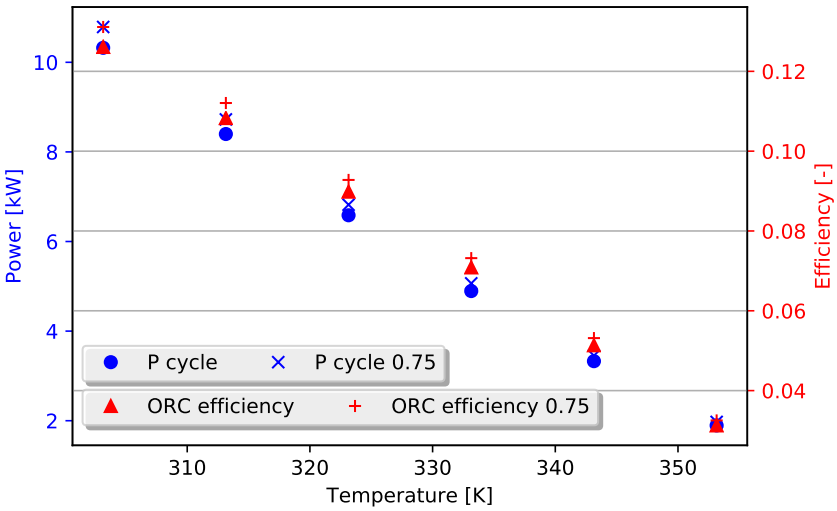

Figure 11: ORC cycle net power (P_{cycle}) and efficiency (η_{cycle}) as a function of the condensation temperature, for fixed mass flow rate (0.7 kg/s), superheat (50 K), vaporization temperature (368.15 K), degree of regeneration (0.9), specific speed (0.6) and specific diameter (3).

Figure 11 shows that both the efficiency of the ORC cycle and the power output are greatly affected by the condensation temperature. In fact, it is well known that a lower value of the condensation temperature has a beneficial effect on the performance of ORC systems. The full dots show that the use of the model presented in this work to evaluate the performance of ORC systems results in lower values for the cycle's efficiency and power output with respect to considering a constant value of 0.75 for the isentropic efficiency of the IFR turbine.

Figures 12 and 13 report respectively the isentropic efficiency of the IFR turbine and the UA coefficient (UA_{sum}) as a function of the specific speed for various values of the vaporization temperature, for fixed mass flow rate (0.7 kg/s), superheat (10 K), condensation temperature (343.15 K), degree of regeneration (0.2) and specific diameter (3.4).

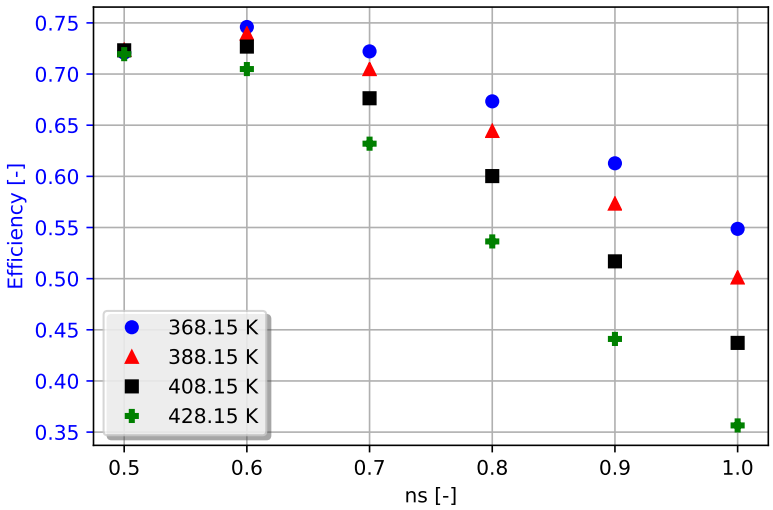

Figure 12: Isentropic efficiency of the IFR turbine as a function of the specific speed for various values of the vaporization temperature, for fixed mass flow rate (0.7 kg/s), superheat (10 K), condensation temperature (343.15 K), degree of regeneration (0.2) and specific diameter (3.4).

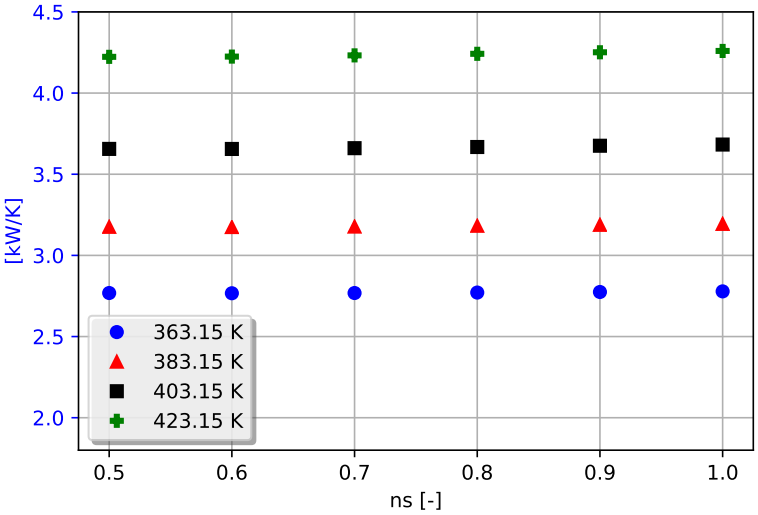

Figure 13: UA coefficient (UA_{sum}) as a function of the specific speed for various values of the vaporization temperature, for fixed mass flow rate (0.7 kg/s), superheat (10 K), condensation temperature (343.15 K), degree of regeneration (0.2) and specific diameter (3.4).

Figure 12 shows that the efficiency of the IFR turbine is greatly affected by the change in the specific speed, as already demonstrated in Figure 7. An increase in the specific speed of the turbine results in a decrease of the efficiency of the turbine, for the given value of

the specific diameter ($d_s = 3.4$, Figure 12). Furthermore, Figure 12 shows that the optimal value of the specific speed, for the given specific diameter, is around 0.55. A decrease in the specific speed below this value results in a decrease of the efficiency of the turbine. Figure 13 shows that the UA parameter, and hence, the size of the heat exchangers is not affected by the specific speed of the turbine. On the contrary, the UA parameter is a strong function of the vaporization temperature of the cycle. In fact, for a given set of conditions of the heat source, the increase in the vaporization temperature of the cycle reduces the temperature difference between the organic fluid at a high pressure and the heat source, resulting in an increase in the size of the heat exchangers. A low vaporization temperature is convenient to enhance the performance of the turbine (see Figure 12) and to minimize the UA coefficient (see Figure 13) but it has a negative effect on the overall ORC efficiency (see Figure 10). A high vaporization temperature ensures an overall higher efficiency at the expenses of a less compact system. A good trade off between the two counteracting effects needs to be found each time an ORC system is designed. This highlights the need for the combined optimization of the design of the IFR turbine and of the ORC cycle parameters proposed in this work.

Figure 14 reports the efficiency of the ORC cycle as a function of the degree of regeneration for various values of the vaporization temperature, for fixed mass flow rate (0.3 kg/s), superheat (30 K), condensation temperature (313.15 K), specific speed (0.6) and specific diameter (3).

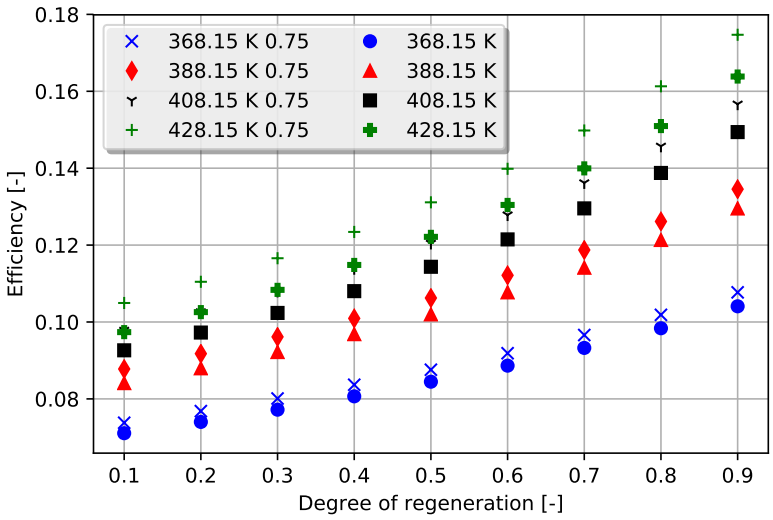

Figure 14: efficiency of the ORC cycle (η_{cycle}) as a function of the degree of regeneration for various values of the vaporization temperature, for fixed mass flow rate (0.3 kg/s), superheat (30 K), condensation temperature (313.15 K), specific speed (0.6) and specific diameter (3).

Figure 14 highlights the discrepancy between the results obtained using the model object of this paper and those obtained by considering a constant 0.75 isentropic efficiency. Also, the beneficial effect of the regeneration on the efficiency of the ORC cycle is assessed. In fact,

regeneration lowers the heat input to the system (i.e. the denominator of Eq. (26)) keeping constant the power output of the system (i.e. the numerator of Eq. (26)). The drawback of regeneration is represented by the addition of a heat exchanger, which - in addition to introducing pressure losses in the cycle - may have a non negligible size and therefore cost. In fact, a regenerator needs to handle liquid on one side and low density vapour on the other side, resulting in a large component. The degree of regeneration is included in the set of decision variables in this work to keep into account its effect on the performance and on the size of the ORC system.

Finally, the percentage error that derives from computing the efficiency of the ORC (η_{cycle}, see Eq. (26)) and of the net power output of the system (P_{cycle}, see Eq. (25)) using a constant isentropic efficiency of 0.75 for the IFR turbine is evaluated. The percentage error ($\%Err$) is expressed as in Eq. (28).

$$\%Err = \frac{|x_{actual} - x_{0.75}|}{x_{0.75}} \dot{1}00 \tag{28}$$

where $x_{0.75}$ is the value calculated considering a constant value for the isentropic efficiency of the IFR turbine of 0.75 while x_{actual} is the value calculated considering the effect of the thermodynamic parameters on the efficiency of the IFR turbine.

Using multiple values for the decision variables, the net power of the cycle (P_{cycle}) and the efficiency of the ORC system (η_{cycle}) have been evaluated considering a constant turbine efficiency of 0.75 in one case and calculating the turbine efficiency via the model proposed in Section 3.2 in the other case. Figure 15 shows the percentage error for the cases analyzed.

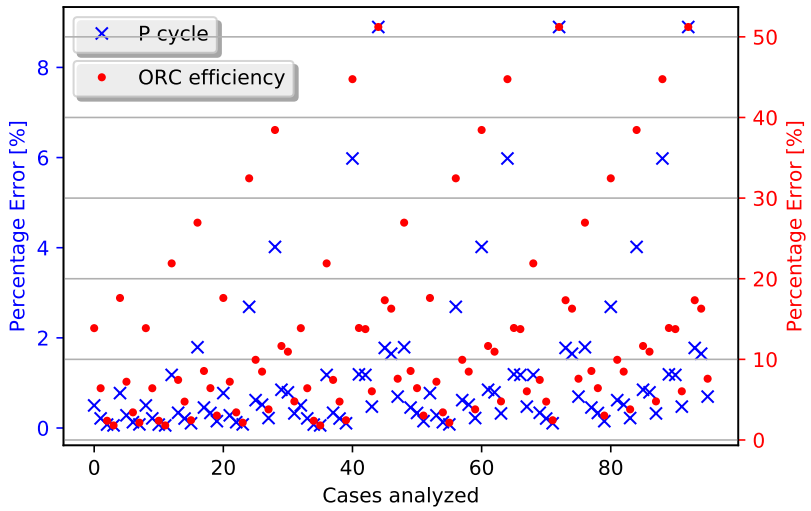

Figure 15: Percentage error in the evaluation of the net power (P_{cycle}) and on the efficiency of the ORC cycle (η_{cycle}) when considering a constant isentropic efficiency for the turbine of 0.75. The calculations have been considered varying the decision variables over a wide range. Specifically, the vaporization temperature (363.15 - 433.15 K) and the specific speed (0.3 - 1.2) have been varied, keeping constant the turbine power (15 kW), the super heating rate (30K), the condensation temperature (310.15 K), the degree of regeneration (0.5) and the specific diameter (3).

.

Figure 15 reports the percentage error when considering a constant isentropic efficiency of the IFR turbine. The blue crosses refer to the percentage error on the calculation of the power of the cycle (P_{cycle}, left y axis) whereas the red dots refer to the percentage error on the calculation of the efficiency of the cycle (η_{cycle}, right y axis). For the cases analyzed, the error on the power output of the cycle reaches values as high as 8 % while the efficiency of the cycle is estimated with a greater error, reaching values that exceed 50%.

Section 4 demonstrates the need for the inclusion of the impact of the thermodynamic parameters on the isentropic efficiency of the turbine at the stage of the selection of the thermodynamic parameters of the cycle. Section 5 reports the results obtained from the application of the ANN optimization approach presented in Section 3. The optimization problems introduced in Section 3.4 have been solved taking into account the impact of the thermodynamic parameters of the cycle on the performance of the IFR turbine.

5. Optimization of the performance of an organic Rankine cycle system using the neural network approach

Section 5 presents the application of the optimization model described in Section 3 to the optimization of an ORC system for waste heat recovery applications.

The ORC system to be designed is conceived to recover the thermal energy released in the exhaust gasses of a 206 kW $YC6A280-30$ Yuchai engine. A thermal oil loop extracts

the thermal energy discharged by the engine in the exhaust gasses via a shell and tube heat exchanger. At steady state conditions, the thermal oil in input to the ORC reaches a temperature of 493.15 K and a mass flow rate of 0.67 kg/s and the minimum temperature that the oil can reach is 418 K, to avoid that the exhaust gasses reach the dew point. Notice that the optimization performed in this paper represents the first step taken in the design of the prototype of an ORC test rig that has been presented and tested in [23].

The use of surrogate models derived by means of the machine learning approach as introduced in this paper represents a promising technique to solve the highly nonlinear optimization problems (24) presented in Section 3.4. In fact, neural network models provide a continuously differentiable correlation function as the one presented in Eq. (1), that makes it possible the use of gradient based methods for the optimization process. The use of gradient methods, as opposed to derivative-free methods commonly used in ORC optimization problems (e.g. genetic algorithms), allows to reach more accurate results in an amount of time that is one order of magnitude smaller [12].

The target set for the ANN models has been derived using the thermodynamic models described in Section 3, that have been developed using the software MATLAB [15]. In particular the target set has been obtained running the physical model multiple times for different values of the decision variables listed in Table 3 in the ranges reported in Table 4 (order of 10^5 samples).

Table 4: Range of the inputs for which the neural network is trained.

Parameter	Value
$\dot{m}_{wf}$ [kg/s]	$0.2 - 1$
T_4 [K]	$368.15 - 438.15$
$\Delta T_{sh} = T_5 - T_4$ [K]	$10 - 90$
T_7 [K]	$303.15 - 353.15$
RD [-]	$0.05 - 0.95$
n_s [-]	$0.5 - 0.7$
d_s [-]	$3.5 - 6$

For the purpose of this work, 19 networks have been trained using the input variables of Table 3 in the range reported in Table 4. Each network has been trained to predict a different output; three networks are representative of the three objective functions of the optimization problems presented in Section 3.4. The remaining 15 networks are meant to describe the constraints c_i of the optimization problems (27) introduced in Section 3.4. As a matter of example, the first constraint of the optimization problems (24) is written as

$$c_1 = T_1 - T_{1,cf} - \Delta T \geq 0 \tag{29}$$

The output of the neural network representing the first constraint is the function c_1. The same has been done for the remaining 14 constraints of the optimization problems (24).

The optimization problems (24) have been solved using both the Neural Network models presented in Section 2 and standard derivative-free algorithms to compare the performance of the different optimization techniques both in terms of accuracy and computational time. In particular, two different derivative-free optimization algorithms have been used in this work. First, the Mesh Adaptive Direct Search (MADS) method as implemented in the OPTI toolbox [24] and presented by the authors in [12]. Second, genetic algorithms (GAs) as implemented in the optimization toolbox of the software MATLAB [15], which are derivative-free optimization algorithms of the class of evolutionary algorithms. Because of their ease of implementation, GAs are broadly used, even when more suitable optimization algorithms would be more performing.

When machine learning models are used, the solution of the optimization problems (24) requires two steps:

1. The training of the Neural Networks representing the objective functions f_j and the constraints c_i;

2. The solution of the optimization problem.

The set of 18 networks has been used to solve two different categories of optimization problems. First, the multi-objective optimization via scalarization to single optimizations of the three objective functions has been performed. Second, the same optimization problems have been solved using holistic scalarization techniques. In both cases, the objective functions are subject to the constraints c_i .

Section 5 is divided into three parts. Section 5.1 reports the sensitivity analysis over the performance of different architectures of the neural networks, to identify the structure that maximizes the accuracy of the predictions. Section 5.2 reports the results of the multi-objective optimization via scalarization to single optimizations when using the proposed surrogate models based on the ANN approach in comparison with those obtained using standard derivative-free algorithms. It is demonstrated that the results one can obtain using the neural network approach are consistent to those commonly found using alternative optimization methods and that the computational effort required is lower. Section 5.3 considers two possible holistic scalarization methods for the solution of the multi-objective optimization problems that are solved by means of the surrogate ANN models to investigate both the performance of the algorithm and the design optimization results with respect to those obtained by the single objectives optimization.

5.1. Choice of the architectures and parameters of the neural networks

All the neural networks used to approximate the functions in the optimization problems (24) are coded using TensorFlow [13], an open source software library for machine learning applications. A different neural network is defined for each of the output functions that must be approximated f_j, $j = 1, 2, 3$ and c_i, $i = 1, \ldots, 15$.

The training phase, as already mentioned in Section 2, consists in solving an optimization problem in which the objective is the minimization of the error of the network in evaluating known examples. The mean squared error has been considered as the function to be minimized during the training phase. The algorithm used for the optimization is Adam [25], a modified stochastic gradient descent with a mini-batch of dimension 500. An initial learning rate of 0.01 and a maximum number of epochs of 200 have been selected for the training phase.

Different architectures of the network have been considered with different activation functions g as the sigmoid, the hyperbolic tangent and the $ReLu$. The selected activation function at the end is the sigmoid function g(t):

$$g(t) = \frac{1}{1 + e^{-t}} \tag{30}$$

that results in better performance.

Different configurations of the network have been tested both shallow and deep using a trial and error process to determine the number of hidden layers and of the neurons. Generally speaking, the larger the number of parameters, i.e. units of the network, the larger must be the target set used in the training phase, otherwise overfitting can easily occur.

For the case of this work, the training set is derived running multiple times the analytical code presented in Section 3, so that one can generate a training set of a large number of instances, at the expenses of a time consuming learning process. However it has been decided to limit the size of the training set to guarantee a good trade off between the computational time required for the training process and the accuracy of the solution.

Different configurations of the network have been tested, to investigate the performance of the different networks and select the best setting to be used in the optimization problems. Specifically, shallow structures of the network have been considered, respectively with 20, 50 and 100 neurons in the hidden layer and a deep network with two hidden layers with 30 neurons in the first layer and 10 neurons in the second one.

The training phase has been implemented as a k-fold cross validation procedure (with $k = 10$) that consists in using 90% of the data as training set and the remaining 10% as the validation set used to evaluate key performance indicators (KPIs). This is a well known procedure which allows to use all the available samples for the prediction without being biased by the choice of the splitting in training versus test sets. The overall performance of the different architectures is measured as the average of the obtained KPIs. In particular the average relative absolute error has been used to compare the predictions of the different networks. The results are reported in Table 5 where each row refers to the Neural Network representing one of the output functions, being the first three lines those corresponding to the three objective functions (P_{cycle}, η_{cycle} and UA_{sum}) and the remaining lines those related to the constraints (c_1 to c_{15}). Each column represents the 10-fold cross validation relative absolute error obtained by the different configuration of the networks.

The last column "Winner" of Table 5 reports the configuration that gives the best relative absolute error. A "tie" is declared when the values differ at most of the 0.01%.

Table 5: 10−fold cross average relative absolute error.

Network	20 N	50 N	100 N	30 - 10 N	Winner
$f_1 = P_{cycle}$	0.017	0.0129	0.0158	0.0075	30-10
$f_2 = \eta_{cycle}$	0.0159	0.014	0.0117	0.0109	tie
$f_3 = UA_{sum}$	0.032	0.039	0.0302	0.0105	30 - 10
c_1	0.0021	0.00478	0.0207	0.0016	30 - 10
c_2	0.0024	0.00478	0.0143	0.00137	tie
c_3	0.4811	0.484	0.4828	0.483	tie
c_4	0.0023	0.0031	0.0053	0.0023	tie
c_5	0.006	0.0067	0.0146	0.0072	30 - 10
c_6	0.0074	0.0129	0.0143	0.0049	30 - 10
c_7	0.0035	0.0059	0.0123	0.0041	tie
c_8	0.29	0.289	0.289	0.2899	tie
c_9	0.0076	0.007	0.0193	0.00587	30 - 10
c_{10}	0.0058	0.0089	0.0211	0.0048	tie
c_{11}	0.309	0.308	0.309	0.31	tie
c_{12}	0.0029	0.0036	0.0082	0.0029	tie
c_{13}	0.0059	0.0058	0.011	0.0068	tie
c_{14}	0.0053	0.0086	0.0119	0.0069	tie
c_{15}	0.0068	0.012	0.0116	0.0071	tie

It has been decided to select the same type of network for all the functions to be approximated f_j and c_i. From the results in Table 5, the configuration that has the best predictive performance is the deep network with two hidden layers, so that it has been selected for the construction of the surrogate models necessary to solve the optimization problems (24).

5.2. Multi Objective optimization via scalarization and comparison among algorithms

In this Section the optimization problems presented in Section 3.4 are solved by using either the surrogate models obtained by the deep Neural Networks chosen in Section 5.1 with a gradient based method, or the black box model with standard derivative-free methods.

The multi-objective optimization problems have been solved by means of a scalarization procedure that falls under the category of ϵ - constraints multi-objective optimization of the following form:

$$\begin{aligned} \min_{x \in \Omega} \quad & f_l(x) \\ & c(x) \leq 0 \\ & f_i(x) \leq \epsilon_i \ \forall \ i = i, ..., k \ i \neq l \end{aligned} \tag{31}$$

where $f_l(x)$ is the function chosen to be optimized whereas $f_i(x)$, $i \neq l$ are the remaining objective functions that are instead add as constraints with a given tolerance ϵ_i to the other constraints $c(x) : \mathbb{R}^n \to \mathbb{R}^{15}$ of the problem.

In particular, the following procedure has been adopted.

First, the problem P_1 of maximizing the net power output f_1 of the ORC system has been solved obtaining the value $\widehat{x}^1$:

$$\begin{aligned} \widehat{f_1} = \min_{\mathbf{x}\in\Omega} \quad & f_1(x) \\ \text{s.t.} \quad & c_i(x) \leq 0\,,\ i = 1,\ldots,15 \end{aligned}$$

where the constraint on the minimum power output is removed.

Subsequently, the maximization of the efficiency of the cycle f_2 and the minimization of the UA parameter f_3 have been solved with the additional constraint that the net power output f_1 of the ORC is at least 90 % of $\widehat{f_1}$; namely the solutions $\widehat{x}^2$, $\widehat{x}^3$ of the two problems P_2 and P_3 have been obtained as:

$$\begin{aligned} \widehat{f_2} = \min_{\mathbf{x}\in\Omega} \quad & f_2(x) \\ \text{s.t.} \quad & c_i(x) \leq 0\,,\ i = 1,\ldots,15 \\ & c_{16} = 0.9\widehat{f_1} - f_1(x) \leq 0 \end{aligned} \qquad \begin{aligned} \widehat{f_3} = \min_{\mathbf{x}\in\Omega} \quad & f_3(x) \\ \text{s.t.} \quad & c_i(x) \leq 0\,,\ i = 1,\ldots,15 \\ & c_{16} = 0.9\widehat{f_1} - f_1(x) \leq 0 \end{aligned}$$

The three single optimization problems P_i, $i = 1, 2, 3$ have been solved by either the derivative-free methods (i.e. MADS and GA) or by using the ANN surrogate models and the algorithm SLSQP [26] as implemented in SciPy [27] (SANO: Surrogate Artificial Network Optimization). It is noted that, due to non convexity, it is not possible to certificate that a global solution is reached. However, to improve the quality of the solution a simple global strategy based on a random multi-start algorithm using 20 random starting points has been used. The best solution obtained after 20 runs of the multi-start SLSQP algorithm is selected.

Table 6 reports the results of the optimizations. In particular for each of three single-objective problems P_i, $i = 1, 2, 3$ defined above, the results obtained by using the GA, MADS algorithm and the proposed SANO are reported.

For each problem P_i, $i = 1, 2, 3$, and for each algorithm GA, MADS or SANO the following values are reported:

- the value of the optimal decision variables $\widehat{x}^i$;
- the values of the three objective functions $f_j(\widehat{x}^i)$ for $j = 1, 2, 3$ (in bold $j = i$);
- the corresponding isentropic efficiency of the IFR turbine η_{is};
- the computational time (cpu time) required for the optimization.

Table 6 shows that the GA, one of the optimization algorithms most commonly used for the optimization of ORC systems, provides the worse performance among the three optimization methods. In fact, the optimal values found using the GA in the solution of

Table 6: Optimization results.

Parameters	P_1 ($\max P_{cycle}$)			P_2 ($\max \eta_{cycle}$)			P_3 ($\min UA_{sum}$)		
	GA	MADS	SANO	GA	MADS	SANO	GA	MADS	SANO
$\dot{m}_{wf}$ [kg/s]	0.84	0.95	0.93	0.86	0.83	0.82	0.9	0.92	0.88
T_4 [K]	437	437	438	438	438	438	438	430	438
ΔT_{sh} [K]	41	33	34	39	42	42	36	33	32
T_7 [K]	326	328	328	326	325	325	327	327	327
RD [-]	0.85	0.9	0.88	0.91	0.91	0.9	0.9	0.85	0.82
n_s [-]	0.5	0.5	0.5	0.5	0.5	0.5	0.5	0.5	0.5
d_s [-]	3.5	3.5	3.5	3.5	3.5	3.5	3.5	3.5	3.5
P_{cycle} [kW]	**15.39**	**16.33**	**16.07**	15.62	15.25	15.24	15.93	15.25	15.247
η_{cycle} [-]	0.15	0.15	0.149	**0.157**	**0.159**	**0.159**	0.15	0.141	0.141
UA_{sum} [kW/K]	14.23	16.29	15.36	15.25	14.85	14.74	**15.68**	**13.19**	**12.79**
η_{is} [-]	0.69	0.70	0.70	0.69	0.69	0.69	0.7	0.71	0.7
Cpu time [s]	6441.7	165	4.1	6663	103	8.4	6304	432	5.2

the three optimization problems is worse with respect to the values found by the other two methods using significantly more computational time. Hence we can limit the discussion to the comparison beetween MADS and SANO.

Table 6 shows that the computational time required to solve the optimization problems using SANO with the multistart procedure is two orders of magnitude smaller than that needed by the MADS algorithm. However one may argue that the time comparison is not fair in that the most time consumed when using the SANO approach is due to the training of the networks. Actually, the overall time required to train each network, in the proposed setting, is of the same order of magnitude of the time needed to solve each optimization problem by the MADS algorithm. Furthermore, in ORC design multiple optimization problems need to be solved to take a decision on the final design of the system. Therefore, the SANO approach results promising. In fact, if the design of the system requires the solution of more than 19 optimization problems (equal to the number of networks trained in the proposed methodology), the SANO approach proposed results in time saving that increases exponentially with the number of optimization problems solved. For what concern the maximization of the net power output of the ORC system (see Table 6), the optimal value of the specific speed (n_s) results to be one that maximizes the turbine efficiency (see Figure 7) and the optimal value of the vaporization temperature results to be the maximum possible. As already discussed in this work, a high value of the vaporization temperature has a negative impact on the isentropic efficiency of the IFR turbine (see Figure 8) and a positive impact on the cycle's efficiency (see Figure 10). The results of Table 6 show that, with the objective of maximizing the net power output of the ORC cycle, the cycle's efficiency has a higher impact with respect to that of the IFR turbine.

A physical interpretation of the results leads to the conclusion that, to improve the efficiency of the ORC cycle, one needs to increase the degree of regeneration and the superheat. The optimal values for the specific speed and the specific diameter of the IFR turbine are not varied with respect to the case of the optimization of the net power output of the cycle. It is worth mentioning that the same value for the n_s and the d_s parameter does not imply

that the IFR turbine has the same rotational speed and diameter in the two cases. In fact, the rotational speed and the diameter of the rotor of the turbine are a function of the thermodynamic conditions at the inlet and at the outlet of the turbine, which are different in the two optimization problems considered. One can conclude that the IFR turbine to maximize the net power output of the system and that necessary to maximize the thermodynamic efficiency of the cycle present a different design.

The SANO approach provides an optimal value for the UA parameter that is lower than that found with MADS method (see Table 6). This demonstrates that the higher the non linearity of the model to be optimized, the more accurate the solution found using surrogate machine learning models with respect to the use of a derivative-free algorithm. From a thermodynamic stand point, one may notice that the minimization of the UA parameter, which is directly proportional to the size of the ORC system, can be obtained diminishing the degree of regeneration, since the regenerator represents the heat exchanger with the largest dimensions of an ORC system.

5.3. A holistic formulation of the multi-objective optimization of the ORC system

The results listed in Table 6 referring to the different optimization problems proposed in Section 3.4 lead to a set of different values for the decision variables, which in turn, implies the design of three different ORC systems, each representing the optimal solution for a specific purpose. The choice of one of the optimal solution requires the supervision of an expert who takes into account additional a posteriori preferences criteria.

In this section, a holistic multi objective optimization approach has been considered to investigate over the optimal configuration that would result from keeping into account the three objective functions (i.e. P_{cycle}, η_{cycle} and UA_{sum}) at the same time. This has been done using two alternative methodologies: goal programming, which is a method without preferences, and weighted sum method, which instead requires a priori preferences.

First, goal programming [28] has been used, which is based on the assumption that the different objective functions are treated in the same way.

Goal programming consists in solving the optimization problem described in (32):

$$\begin{aligned} \min_{\mathbf{x}\in\Omega} \quad & ||f(x) - z_{id}||_p \\ & c(x) \leq 0 \end{aligned} \tag{32}$$

where $||\cdot||_p$ is the ℓ_p norm of a vector, with $1 \leq p \leq \infty$ and z_{id} is a reference point. For the specific purpose of this work, z_{id} is represented by the optimal values resulted from the resolution of the optimization problems discussed in the previous Section, namely the optimal values P_{cycle}, η_{cycle} and UA_{sum} obtained by SANO for problem P_1, P_2 and P_3 respectively and reported in bold in Table 6.

The problem (32) aims at minimizing the difference between the optimal solutions of the optimization problems reported in Table 6 and those of the holistic multi objective optimization. Different results are obtained for different values of the norm p. The optimization has been performed using the SANO method and the algorithm SLSQP. Table 7 reports the

results of the multi-objective optimization problem, solved using goal programming with different values of p.

Table 7: Multi Objective Optimization using the goal programming approach with $p = 1, 2, \infty$.

Parameters	$p = 1$	$p = 2$	$p = \infty$
$\dot{m}_{wf}$ [kg/s]	0.78	0.83	0.85
T_4 [K]	437	438	438
ΔT_{sh} [K]	40	36	35
T_7 [K]	324	325	326
RD [-]	0.91	0.88	0.87
n_s [-]	0.5	0.5	0.5
d_s [-]	3.5	3.5	3.5
P_{cycle} [kW]	14.47	14.94	15.21
η_{cycle} [-]	0.159	0.153	0.15
UA_{sum} [kW/K]	13.17	13.26	13.45
η_{is} [-]	0.696	0.697	0.697
Cpu time [s]	15.3	6.71	11.2

Table 7 demonstrates that, depending on the choice of the parameter p, the optimal point assumes different values. It is important to mention that the solution of the goal programming is a Pareto solution when the parameter p assumes finite values. The statement could be false in case the parameter p is infinite (last column, Table 7). The solution obtained using $p = 1$ demonstrates that it is possible to reach the same optimal values listed in Table 6 for what concern the cycle's efficiency and the UA parameter, if one accepts a lower value for the net power output of the cycle. On the contrary, when assuming $p = 2$ and $p = \infty$, the resolution of the holistic multi-objective optimization problems leads to a higher net power output of the cycle with respect to the case $p = 1$, at the expenses of the degradation of the remaining objective values, i.e. the cycle's efficiency and the UA parameter. An alternative methodology to perform multi-objective optimization is the weighted sum method [29], which consists in allowing the decisor to rank the different objective functions in order of preference. This leads to an optimization problem of the form (33):

$$\begin{aligned} \min_{\mathbf{x}\in\Omega} \quad & \sum_{i=1}^{k} w_i \cdot f_i(x) \\ & c_i(x) \leq 0 \quad i = 1, \ldots, 15 \end{aligned} \tag{33}$$

where the weights $w_i \geq 0$ are normalized, i.e. they satisfy the condition of Eq. (34):

$$\sum_{i=1}^{k} w_i = 1 \tag{34}$$

it is well known that the solution obtained by the weighted sum method is a Pareto solution.

Table 8 reports the solution of the multi-objective optimization problem using the weighted sum method, with the objective function defined as:

$$\min_{\mathbf{x}\in\Omega} \quad (-w_1 P_{cycle} - w_2 \eta_{cycle} + w_3 UA_{sum})$$

and assuming different values for the weights.

Table 8: Multi Objective Optimization using the weighted sum method.

Parameters	$w_1 = 0.7$ $w_2 = 0.2$ $w_3 = 0.1$	$w_1 = 0.5$ $w_2 = 0.4$ $w_3 = 0.1$	$w_1 = 0.5$ $w_2 = 0.1$ $w_3 = 0.4$
$\dot{m}_{wf}$ [kg/s]	0.93	0.83	0.84
T_4 [K]	438	438	438
ΔT_{sh} [K]	34	41	17
T_7 [K]	328	325	330
RD [-]	0.87	0.9	0.66
n_s [-]	0.5	0.5	0.5
d_s [-]	3.5	3.5	3.5
P_{cycle} [kW]	16.07	15.32	13.19
η_{cycle} [-]	0.149	0.158	0.119
UA_{sum} [kW/K]	15.36	14.8	8.77
η_{is} [-]	0.7	0.697	0.7
Cpu time [s]	2.77	4.57	3.54

The results shown in Table 8 report three different Pareto solutions obtained by setting different values for the weights. In the first setting, high priority is given to the weight referring to the net power production (i.e., w_1), in that the ORC proposed is conceived for waste heat recovery applications where the maximization of the net power production is crucial. In this case, the Pareto solution turns out to be very similar to the one obtained by the maximization of the power output reported in Table 6. The other two settings of weights reduce the weight associated with the net power production, increasing in turns the weight of the efficiency of the cycle (i.e. w_2) and of the UA parameter (i.e. w_3). An increase of w_2 has a beneficial effect on the value found for the cycle's efficiency and for the UA parameter with respect to the first case analyzed. The increase of w_3 leads to a substantial reduction of the UA parameter (and hence, a reduction of the size of the ORC system) at the expenses of a lower net power production and efficiency.

The weighted sum method results particularly suitable to plot a set of Pareto solutions when considering only two objective functions at a time. In the rest of this Section, different

plots show the results of multi-objective optimization problems in which two of the three objective functions are taken into account simultaneously, assigning a null value to the weight of the third objective function. In other words, each Figure presents the results obtained solving the problem:

$$\begin{array}{ll} \min & w_i f_i + w_j f_j + w_k f_k \\ s.t. & c_h \leq 0, \ h = 1, \ldots, 15 \end{array}$$

where the weights assume the values:

Opt. Problem	1	2	3	4	5	6	7	8	9	10	11
w_i	1	0.9	0.8	0.7	0.6	0.5	0.4	0.3	0.2	0.1	0
w_j	0	0.1	0.2	0.3	0.4	0.5	0.6	0.7	0.8	0.9	1
w_k	0	0	0	0	0	0	0	0	0	0	0

Each Figure shows the Pareto solutions obtained by solving 11 optimization problems corresponding to the following assignments of the subscripts:

Figure	16	17	18
P_{cycle}	j	k	i
η_{cycle}	i	j	k
UA_{sum}	k	i	j

Figure 16 shows the Pareto front in the objective space of the efficiency and the power output of the cycle.

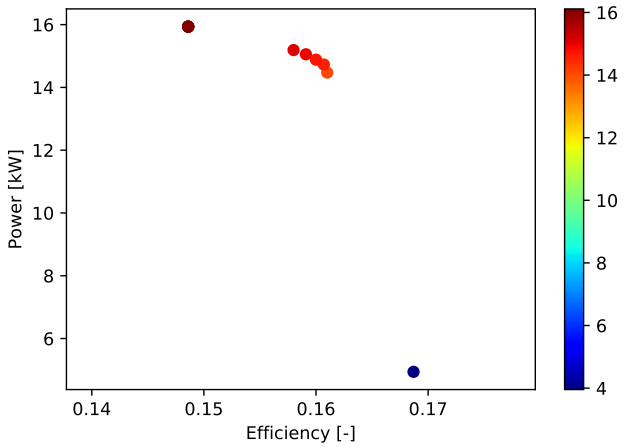

Figure 16: Pareto front in the objective space of the efficiency (η_{cycle}) and the power output of the cycle (P_{cycle})

Figure 16 demonstrates that the maximum efficiency of the system (blue dot, bottom right) can be obtained at the expenses of a low power output. In a waste heat recovery application, in which one would like to produce as much electricity as possible from a given amount of thermal energy, the aforementioned design point does not represent an interesting solution. On the other hand, the configuration which is capable of extracting the maximum amount of power (dark red, top left) shows the lowest efficiency and the highest UA_{sum} among the configurations analyzed. Figure 16 suggests that a trade off between efficiency and power needs to be found.

Figure 17 shows the Pareto front in the objective space of the efficiency of the cycle and the UA parameter.

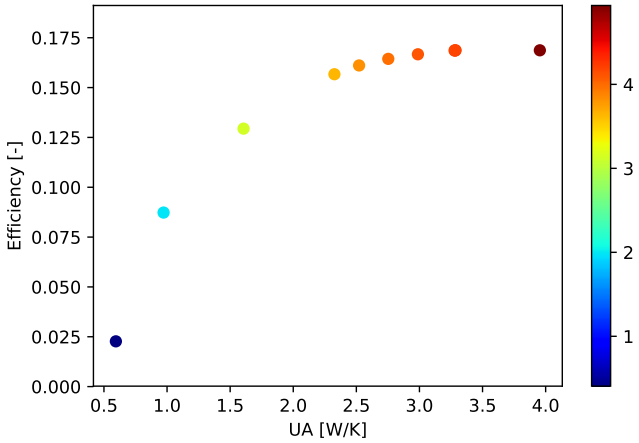

Figure 17: Pareto front in the objective space of the efficiency of the cycle (η_{cycle}) and the UA parameter (UA_{sum})

Figure 17 demonstrates that the efficiency and the UA_{sum} parameter are conflicting objectives. In fact, a high efficiency of the system is obtained for a large UA_{sum} value and viceversa. It can also be observed that the improvement in the efficiency with an increase of the UA_{sum} parameter follows a non-linear trend. Figure 17 highlights that increasing the UA_{sum} parameter has limited effect on the efficiency for values of the UA_{sum} parameter higher than 3 W/K.

Figure 18 shows the Pareto front in the objective space of the power output of the cycle and the UA parameter.

Figure 18 shows that the value of the UA_{sum} parameter, directly correlated to the size of the system, increases almost linearly with the power output of the system. In other words, the reduction of the size of the system implies a decrease of the power output. The results reported in Figure 18 can be used to take decisions on the power output of the system in those cases in which the size of the system is constrained.

The results show that the introduction of the SANO approach allows for the representation of a portion of the Pareto front. This would take a consistently larger amount of time using traditional optimization techniques that do not provide an analytic model.

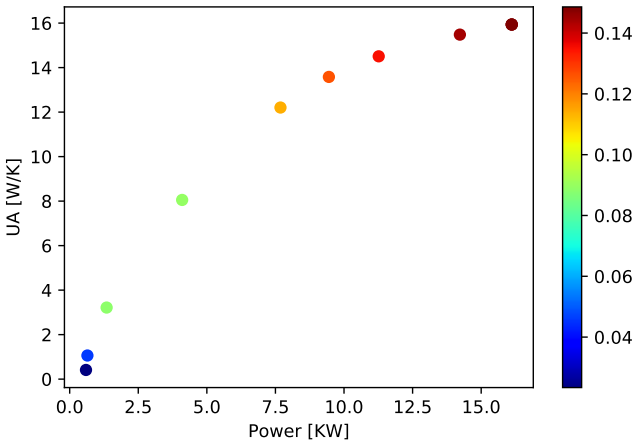

Figure 18: Pareto front in the objective space of the power output of the cycle (P_{cycle}) and the UA parameter (UA_{sum})

Section 5.3 demonstrates that depending on the strategy considered to perform the multi-objective optimization one may found a different Pareto solution. The experience of the designer drives the choice among the different optimized configurations.

6. Conclusions

This work proposes a novel methodology based on machine learning techniques for the combined optimization of the thermodynamic cycle and of the radial in-flow turbine for small scale Organic Rankine cycle applications. The machine learning approach consists in converting the physical model of the thermodynamic cycle and of the components of the plant into a set of continuous and differentiable functions. This approach allows for the use of gradient based methods for the optimization, as opposed to derivative-free methods, and this leads to an increase in the accuracy of the solution and to a decrease of the computational time required to solve the optimization problem.

The results of this work can be summarized as follows:

- The combination of the design of the thermodynamic cycle and that of the radial inflow turbine leads to an increase in the accuracy in the prediction of the performance of the system of up to 8 % for what concern the power output of the system and up to 50 % for the efficiency of small scale Organic Rankine cycle systems;

- Different architectures of the neural network have been tested, showing that the required number of neurons in the hidden layer to obtain accurate predictions strongly depends on the objective function to be optimized. The 2-layers network has been used because it is the one that shows the lowest error in predicting the instances of the test set;

- The neural networks designed in this work show that they are capable of accurately learning the highly nonlinear physical model object of this work with a degree of accuracy higher than 99 %;
- The proposed neural network approach proved more efficient than derivative-free algorithms in the optimization of Organic Rankine cycle systems, reaching an accurate solution in a computational time that is two orders of magnitude lower than that of derivative-free methods. This depends on the possibility to use gradient methods for the optimization, once the physical model is mathematically converted into a set of functions suitable for the optimization;
- The maximization of the net power output of the system is obtained by maximizing the vaporization temperature of the cycle and selecting a specific speed value of 0.5 for the radial in-flow turbine;
- The maximization of the efficiency of the cycle is reached through the maximization of the degree of regeneration and the increase of the superheat with respect to that of the maximization of the net power output of the cycle;
- The minimization of the size of the heat exchangers is reached through a minimization of the degree of regeneration, since the regenerator is by far the largest heat exchanger in an Organic Rankine cycle system;
- The multi-objective optimization strategies considered can be conveniently used in the design process of small scale systems. The strategy considered for the multi-objective optimization plays a crucial role in the definition of the Pareto solution reached.

The machine learning approach for the combined optimization of the thermodynamic parameters of the Organic Rankine cycle and of the design parameters of the in-flow radial turbine represents a promising alternative to the most commonly used derivative-free optimization algorithms. The higher accuracy in the results and the substantially shorter computational time required for the optimization process make the proposed approach ideal for the solution of many highly nonlinear problems, typical of the energy field.

This paper represents the first step towards the design of an optimization tool that can be used by academics and industries for the design multi-objective optimization of Organic Rankine cycle systems. The rapid evaluation of a large set of possible (i.e. feasible) design configurations provides the opportunity to explore different optimization criteria before taking final decisions of the ORC system to be built.

Acknowledgments

Entropea Labs is acknowledged for the economic and technical support provided during the completion of this study.

Abbreviations

ANN	Artificial Neural Network
CoMT-CAMD	Continuous-Molecular Targeting Computer Aided Molecular Design
GA	Genetic Algorithm
HL	Hidden Layer
IFR	In-Flow Radial
IL	Input Layer
KPI	key performance indicator
MADS	Mesh Adaptive Direct Search
NTU	Net Transfer Unit
OL	Output Layer
OPTI	OPTimization Interface
ORC	Organic Rankine Cycle
SANO	Surrogate Artificial Network Optimization
SLSQP	Sequential Least Square Quadratic Programming

Nomenclature

A	Area	$[m^2]$
α	angle of the blades	[degrees]
b	threshold	[-]
$b_{r,in}$	thickness of the blade of the turbine	[m]
c	constraint	
c_p	specific heat at constant pressure	[J/kgK]
C	thermal capacity	[J/sK]
d_s	specific diameter	[-]
D	diameter	[m]
ΔT	pinch point temperature difference	[K]
ϵ	effectiveness	[-]
η	efficiency	[-]
ϕ_c	flow coefficient Chain and Baines	[-]
g	activation function	[-]
h	enthalpy	[J/kg]
$\dot{m}$	mass flow rate	[kg/s]
m	number of neurons in the hidden layer	[-]
n	number of inputs of the network	[-]
n_s	specific speed	[-]
ω	rotational speed	[rpm]
p	pressure	[Pa]
P	Power	[kW]
ρ	density	$[kg/m^3]$
RD	degree of regeneration	[-]
s	specific entropy	[J/kgK]
ψ	head coefficient	[-]
Q	volumetric flow rate	$[m^3/s]$
tan	tangent	
T	temperature	[K]
U	heat transfer coefficient	$[W/m^2]$
$\vec{U}$	peripheral velocity	[m/s]
$\vec{V}$	absolute velocity	[m/s]
x	vector of inputs	[-]
w	weight	[-]
W_{Euler}	Euler work	[J]
y	target function	[-]
Z	number of blades	[-]
z_{id}	reference point	[-]

Subscripts

c	Chain and Baines
cf	cooling fluid
$cond$	condensation
dsh	de-super heating
$evap$	evaporation
hs	heat source
i	input of the neural network
in	inlet section of the turbine
j	neuron of the hidden layer
is	isentropic
o	output of the neural network
out	outlet section of the turbine
p	instance of the training set
ph	pre heating
r	rotor
reg	regeneration
s	stator
sc	sub cooling
sh	super heating
v	volute
wf	working Fluid
$2p$	two phase

References

[1] S. Quoilin, M. Van Den Broek, S. Declaye, P. Dewallef, V. Lemort, Techno-economic survey of organic rankine cycle (orc) systems, Renewable and Sustainable Energy Reviews 22 (2013) 168–186.

[2] L. Tocci, T. Pal, I. Pesmazoglou, B. Franchetti, Small scale organic rankine cycle (orc): A techno-economic review, Energies 10 (4) (2017) 413.

[3] A. Uusitalo, T. Turunen-Saaresti, A. Gronman, J. Honkatukia, J. Backman, Combined thermodynamic and turbine design analysis of small capacity waste heat recovery orc, Proceedings of the ASME ORC.

[4] C. A. Ventura, P. A. Jacobs, A. S. Rowlands, P. Petrie-Repar, E. Sauret, Preliminary design and performance estimation of radial inflow turbines: An automated approach, Journal of Fluids Engineering 134 (3) (2012) 031102.

[5] A. La Seta, A. Meroni, J. G. Andreasen, L. Pierobon, G. Persico, F. Haglind, Combined turbine and cycle optimization for organic rankine cycle power systems—part b: Application on a case study, Energies 9 (6) (2016) 393.

[6] L. Zhai, G. Xu, J. Wen, Y. Quan, J. Fu, H. Wu, T. Li, An improved modeling for low-grade organic rankine cycle coupled with optimization design of radial-inflow turbine, Energy Conversion and Management 153 (2017) 60–70.

[7] A. Lazzaretto, G. Manente, A new criterion to optimize orc design performance using efficiency correlations for axial and radial turbines, International Journal of Thermodynamics 17 (3) (2014) 192–200.

[8] H. Saffari, S. Sadeghi, M. Khoshzat, P. Mehregan, Thermodynamic analysis and optimization of a geothermal kalina cycle system using artificial bee colony algorithm, Renewable Energy 89 (2016) 154–167.

[9] H. Xi, M.-J. Li, C. Xu, Y.-L. He, Parametric optimization of regenerative organic rankine cycle (orc) for low grade waste heat recovery using genetic algorithm, Energy 58 (2013) 473–482.
[10] X.-S. Zhang, Neural networks in optimization, Vol. 46, Springer Science & Business Media, 2013.
[11] G. Villarrubia, J. F. De Paz, P. Chamoso, F. De la Prieta, Artificial neural networks used in optimization problems, Neurocomputing 272 (2018) 10–16.
[12] A. Massimiani, L. Palagi, E. Sciubba, L. Tocci, Neural networks for small scale orc optimization, Energy Procedia 129 (2017) 34–41.
[13] M. Abadi, A. Agarwal, P. Barham, E. Brevdo, Z. Chen, C. Citro, G. S. Corrado, A. Davis, J. Dean, M. Devin, et al., Tensorflow: Large-scale machine learning on heterogeneous distributed systems, arXiv preprint arXiv:1603.04467.
[14] I. Goodfellow, Y. Bengio, A. Courville, Deep learning, MIT Press, 2016.
[15] MATLAB, version 8.5.0.197613 (R2015a), The MathWorks Inc., Natick, Massachusetts, USA, 2015.
[16] E. W. Lemmon, M. L. Huber, M. O. McLinden, Nist reference fluid thermodynamic and transport properties—refprop, NIST standard reference database 23 (2002) v7.
[17] C. Hall, S. L. Dixon, Fluid mechanics and thermodynamics of turbomachinery, Butterworth-Heinemann, 2013.
[18] D. Fiaschi, G. Manfrida, F. Maraschiello, Design and performance prediction of radial orc turboexpanders, Applied Energy 138 (2015) 517–532.
[19] H. Chen, N. Baines, The aerodynamic loading of radial and mixed-flow turbines, International journal of mechanical sciences 36 (1) (1994) 63–79.
[20] K. Rahbar, S. Mahmoud, R. K. Al-Dadah, N. Moazami, Modelling and optimization of organic rankine cycle based on a small-scale radial inflow turbine, Energy conversion and management 91 (2015) 186–198.
[21] J. Bao, L. Zhao, A review of working fluid and expander selections for organic rankine cycle, Renewable and Sustainable Energy Reviews 24 (2013) 325–342.
[22] G. Nellis, S. Klein, Heat Transfer, Heat Transfer, Cambridge University Press, 2009.
URL `https://books.google.co.uk/books?id=D4FFiD6hZ94C`
[23] F. Alshammari, A. Pesyridis, A. Karvountzis-Kontakiotis, B. Franchetti, Y. Pesmazoglou, Experimental study of a small scale organic rankine cycle waste heat recovery system for a heavy duty diesel engine with focus on the radial inflow turbine expander performance, Applied Energy 215 (2018) 543–555.
[24] J. Currie, D. I. Wilson, et al., Opti: lowering the barrier between open source optimizers and the industrial matlab user, Foundations of computer-aided process operations 24 (2012) 32.
[25] J. Duchi, E. Hazan, Y. Singer, Adaptive subgradient methods for online learning and stochastic optimization, Journal of Machine Learning Research 12 (Jul) (2011) 2121–2159.
[26] R. E. Perez, P. W. Jansen, J. R. Martins, pyOpt: a python-based object-oriented framework for nonlinear constrained optimization, Structural and Multidisciplinary Optimization 45 (1) (2012) 101–118.
[27] K. J. Millman, M. Aivazis, Python for scientists and engineers, Computing in Science & Engineering 13 (2) (2011) 9–12.
[28] F. Gembicki, Y. Haimes, Approach to performance and sensitivity multiobjective optimization: The goal attainment method, IEEE Transactions on Automatic control 20 (6) (1975) 769–771.
[29] R. T. Marler, J. S. Arora, The weighted sum method for multi-objective optimization: new insights, Structural and multidisciplinary optimization 41 (6) (2010) 853–862.